Chemical Science

ROYAL SOCIETY OF CHEMISTRY

EDGE ARTICLE

View Article Online
View Journal

Cite this: DOI: 10.1039/d6sc00414h

All publication charges for this article have been paid for by the Royal Society of Chemistry

Excimer-mediated multiexciton generation in covalently linked cross foldamers of thiophene-fused perylene bisimides

Weicong Li,[a] Wei Zhang,[*bc] Jiadong Zhou,[d] Linlin Liu,[a] Hongwei Song[*a] and Zengqi Xie[*a]

Singlet fission (SF) is a promising strategy to surpass the Shockley–Queisser limit in organic photovoltaics, but the structural and electronic determinants controlling excimer-mediated multiexciton (ME) generation remain insufficiently understood. Herein, we designed two covalently linked cross foldamers, **CF(4)** and **CF(7)**, based on thiophene-fused perylene bisimide units, with controlled intramolecular chromophore rotational angles (88° and 55°) *via* alkyl chain engineering, while maintaining a constant π–π stacking distance. Steady-state and ultrafast spectroscopy studies revealed that both foldamers undergo excimer-mediated ME generation but with distinct dynamics: weakly coupled **CF(4)** (88°) achieves rapid ME formation in 27 ps, whereas strongly coupled **CF(7)** (55°) stabilizes the excimer, slowing ME formation to 114 ps. These results establish a clear structure–dynamics relationship, demonstrating that rotational angle modulation enables tuning of excimer energetics and SF efficiency, providing a general design strategy for π-conjugated assemblies.

Received 15th January 2026
Accepted 22nd April 2026

DOI: 10.1039/d6sc00414h

rsc.li/chemical-science

Introduction

Singlet fission (SF), a process in which one excited singlet exciton is converted into two triplet excitons, has attracted considerable interest as a promising strategy to surpass the Shockley–Queisser limit in organic photovoltaics.[1,2] Since its initial demonstrations in acene crystals and thin films, SF has been observed across a wide range of π-conjugated molecular assemblies, including covalent dimers, supramolecular aggregates, and solid-state materials, highlighting the role of intermolecular coupling and excited-state energetics in governing multiexciton (ME) generation.[3–6] Recent studies reveal that mixed adiabatic electronic states containing diabatic Frenkel exciton (FE), charge transfer (CT), and triplet pair (TT) components, can mediate SF producing two free triplet excitons.[7–11] Excimer (Ex) formation, once regarded primarily as a non-radiative trap state in strongly coupled H-type dimers, has in certain systems been shown to serve as a dynamic intermediate that can mediate productive excited-state processes under appropriate energetic and environmental conditions.[12,13] In this emerging picture, structural relaxation into an excimer configuration provides an energetically favorable pathway that connects the initial FE state, the transition ME state, and the final two free triplet states, blurring the traditional distinction between "trap" and "gateway".[14–16] Despite this progress, the specific structural and electronic determinants that control excimer-mediated ME generation remain insufficiently understood.

Covalently linked molecular dimers and foldamers provide a particularly powerful platform to disentangle such structure–dynamics relationship, as they allow precise control over intramolecular interchromophore geometry, coupling, and conformational freedom.[17–21] In π-conjugated molecule-based dimers, subtle variations in stacking geometry—such as longitudinal slip, rotation angle, or enforced cofacial alignment—can profoundly alter the sum of coulombic and CT couplings, thereby modulating the nature of the lowest excited states and their subsequent relaxation pathways.[22,23] Within this context, excimer formation has been extensively investigated in perylene bisimide (PBI)-based dimers, where strong coupling often stabilizes mixed FE-CT states that compete with or facilitate ME generation.[8,24] Beyond classical H-and J-type arrangements (Fig. 1a),[25–31] more exotic geometries, including magic-angle stackings,[32,33] null aggregates,[17,34] and cross aggregates[35–38] have recently emerged as promising motifs to weaken coupling while preserving close π–π contact, offering new opportunities

[a]State Key Laboratory of Luminescent Materials and Devices, Institute of Polymer Optoelectronic Materials and Devices, Guangdong Provincial Key Laboratory of Luminescence from Molecular Aggregates, Guangdong Basic Research Center of Excellence for Energy and Information Polymer Materials, South China University of Technology, Guangzhou 510640, P. R. China. E-mail: songhongwei@scut.edu.cn; msxiez@scut.edu.cn

[b]Frontier Institute of Science and Technology, Xi'an Jiaotong University, Xi'an 710049, P. R. China. E-mail: zhangwei1991@ustc.edu.cn

[c]Institute of New Concept Sensors and Molecular Materials, Shaanxi Key Laboratory of New Conceptual Sensors and Molecular Materials, Xi'an Jiaotong University, Xian 710049, P. R. China

[d]School of Chemistry, South China Normal University, Guangzhou 510006, P. R. China

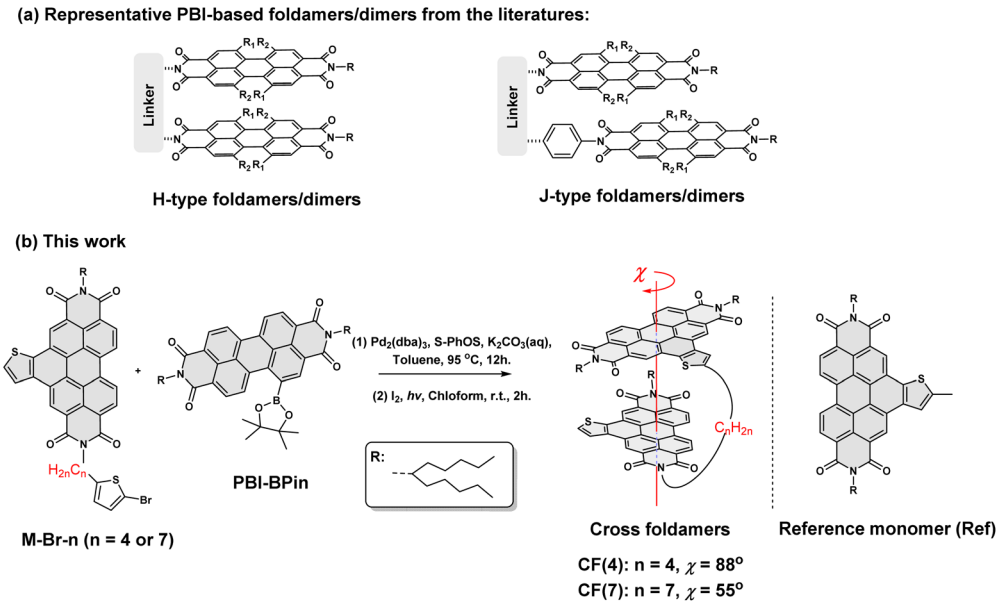

Fig. 1 (a) Representative H-type (ref. 25–28) and J-type (ref. 29–31) PBI-based foldamers/dimers from the literature. (b) Synthesis route of the target cross foldamers **CF(4)** and **CF(7)**. The reference monomer (Ref) is also given for comparison.

to access excimer-mediated ME processes. Despite these advances, general molecular design strategies that enable systematic control of interchromophore rotation over a wide angular range, and that allow direct correlation between rotational geometry, excimer energetics, and SF kinetics, remain limited.[39,40]

Here, we address this challenge using covalently linked, PBI-derivative-based cross foldamers with controlled intrafoldamer interchromophore rotation. We systematically compare a nearly orthogonal foldamer **CF(4)** (88°) and a smaller rotation foldamer **CF(7)** (55°) against a monomer reference (Ref) to elucidate how rotation-modulated coupling governs excimer formation and ME generation dynamics. Both cross foldamers display broad excimer emission and follow an excimer-mediated pathway toward ME. Notably, the dynamics depend strongly on geometry: **CF(4)**, with weaker coupling, enables rapid formation of the ME state, whereas **CF(7)** stabilizes the excimer through CT contributions, creating a deeper potential well that slows ME state formation. These results establish a direct structure–dynamics relationship and demonstrate that linker-length engineering offers a practical handle to tune excimer energetics and optimize SF efficiency in π-conjugated assemblies.

Results and discussion

Molecular structures and steady-state optical properties

We designed two covalently linked dimers of thiophene-fused PBI with varying tether lengths, as shown in Fig. 1b. By connecting the side of one planar π-core to the terminal N position of the other, we aimed to promote intramolecular folding into cross-stacked geometries, stabilized primarily by π–π interactions. The dimers are designated **CF(4)** and **CF(7)** based on the numbers of carbon atoms in the flexible linker. Synthesis of **CF(4)** and **CF(7)** proceeded *via* a two-step route from the precursor monomers PBI-Bpin and M–Br-*n* ($n = 4$ or 7). First, a Suzuki–Miyaura coupling was performed using $Pd_2(dba)_3$ and S-Phos as the catalyst system in toluene (TOL) with K_2CO_3 as base.[41] Subsequent photocyclization, driven by sunlight and catalyzed by iodine, afforded **CF(4)** and **CF(7)** in 46% and 52% yields, respectively.[42] The reference compound (Ref) was also synthesized for comparison (Scheme S1). Full synthetic details and characterization data are provided in SI.

To further elucidate the structural features of the cross-folded architectures, ground-state geometries were optimized at the ωB97X-D/def2-SVP level. For computational efficiency, long alkyl chains on imide positions were replaced with methyl groups. In addition, molecular dynamics (MD) simulations were performed for **CF(4)** and **CF(7)** at 300 K. For each foldamer, a 2 ns trajectory was generated, and snapshots were collected every 1 ps to monitor the evolution of key geometric parameters. The π–π stacking distance was defined as the average perpendicular distance from the plane of all non-hydrogen atoms of one conjugated unit to the plane of the other (Fig. 2a), and the rotational angle was quantified as the cross angle between the N–N axes of the two conjugated units (Fig. 2a). Despite the differing lengths of the linking alkyl chains, both foldamers maintain tight intramolecular stacking, with distances of ~3.3 Å (Fig. S1). As shown in Fig. 2b, the π–π distances remain nearly constant throughout the MD trajectories, yielding similar average values of 3.33 ± 0.06 Å for **CF(4)** and 3.35 ± 0.06 Å for **CF(7)**. The linker-length independence of the stacking distance indicates that the extended conjugated surface effectively stabilizes close π–π stacking in both foldamers. By contrast, the rotational geometries show significant differences (Fig. S1a and b). **CF(4)** adopts a large rotation of 88°, enforced by the shorter

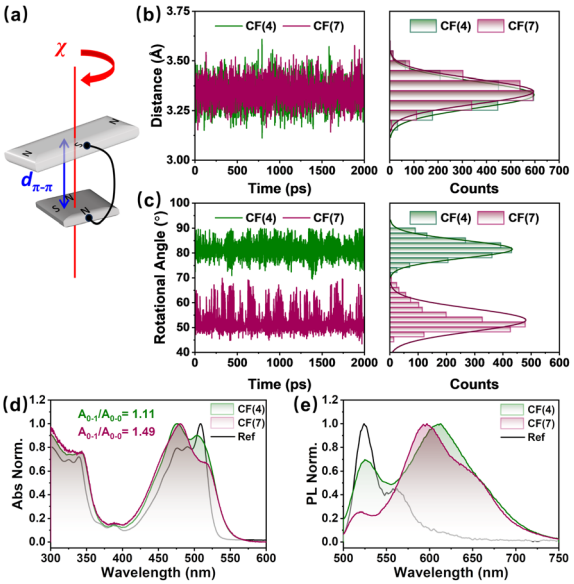

Fig. 2 (a) Schematic representation of a cross foldamer model, illustrating the π−π distance ($d_{\pi-\pi}$) and the relative rotational angle (χ). (b) The π−π distance and (c) the rotational angle at every 1 ps interval over a 2 ns trajectory, shown as time evolution (left) and corresponding distributions (right), traced by MD simulations at 300 K for **CF(4)** and **CF(7)**. (d) Normalized UV-vis absorption and (e) normalized photoluminescence spectra of **CF(4)**, **CF(7)** and Ref in TOL ($c = 1.0 \times 10^{-6}$ M, $\lambda_{ex} = 450$ nm).

alkyl chain, whereas **CF(7)** exhibits a smaller rotation of 55° due to its increased conformational freedom. Rotational-angle distributions produced by MD follow the same trend in Fig. 2c. The close agreement between MD and DFT calculations confirms that elongation of the alkyl chains systematically reduces the rotational angle.

The geometric variations directly modulate exciton coupling. To quantify this effect, the total coupling (J_{Tot}) was calculated as the sum of coulombic coupling (J_{Coul}) and charge-transfer coupling (J_{CT}).[23,43] J_{Coul} and J_{CT} were computed using the density functional theory (DFT) optimized structures *via* a distributed transition-charge method and a superexchange model, respectively (details in SI, Table S2). In the nearly orthogonal geometry of **CF(4)** ($\chi = 88°$), J_{Coul} is strongly suppressed and negative (-138 cm^{-1}), while J_{CT} remains positive yet modest (98 cm^{-1}), resulting in a small J_{Tot} of -40 cm^{-1}. By contrast, **CF(7)** adopts a smaller rotational angle ($\chi = 55°$) and exhibits substantially larger, positive couplings (J_{Coul} = 396 cm^{-1}, J_{CT} = 323 cm^{-1}), yielding a large positive J_{Tot} of 719 cm^{-1}. The negative J_{Coul} in **CF(4)** likely originates from the transition-density effects associated with the thiophene-fused units, while the reduced rotation in **CF(7)** favors positive coulombic coupling. Concurrently, the nearly orthogonal structure in **CF(4)** strongly reduces charge transfer integrals (t_e and t_h, details in SI), limiting the superexchange pathway and resulting in a small J_{CT}. By contrast, the smaller rotation angle in **CF(7)** permits stronger charge transfer interaction. Notably, variations in the rotation angle can lead to significant changes in exciton coupling strength, particularly in CT coupling, enabling excited-state mixing within cross foldamers (*vide infra*). The results demonstrate that modulating the rotational angle provides an effective strategy for controlling both the magnitude and sign of J_{Coul} and J_{CT}, thereby tuning the photophysical character of the foldamer even at a fixed π–π stacking distance.[35,44,45]

To further elucidate structure–property relationship, steady-state absorption and emission spectra of **CF(4)**, **CF(7)** and Ref were recorded in dilute TOL and chloroform ($CHCl_3$) solutions at room temperature (Fig. 2d, e and $CHCl_3$ data in S3). Under these conditions, intermolecular aggregation was ruled out (Fig. S4). Ref exhibits a sharp progression profile with a maximum at 508 nm, corresponding to the $S_0 \rightarrow S_1$ transition, along with several vibronic peaks. Its emission shows clearly resolved vibrational progressions, characteristic of monomeric PBI chromophores (Fig. S5).

By contrast, the absorption spectra of the cross foldamers **CF(4)** and **CF(7)** deviate markedly from that of Ref (Fig. 2d), indicating effective intramolecular interactions between the tethered π-cores. Both foldamers show broadened absorption with enhanced A_{0-1} intensity and a pronounced tail extending into the red-shifted region. The features are consistent with a rotation-stacked geometry that exhibits mixed H- and J-type characteristics, arising from optically allowed transitions among the excitonically split energy levels. Notably, the intensity ratio A_{0-1}/A_{0-0} for **CF(7)** is significantly larger than that for **CF(4)**, which correlates well with the much larger positive J_{Tot} of **CF(7)** *versus* the near-zero coupling in **CF(4)**.

The emission spectra of both foldamers are dominated by broad, featureless, and red-shifted bands between 550 and 750 nm (Fig. 2e) with prolong time-resolved photoluminescence (TRPL) lifetimes (Fig. S8). We assign this band to an intramolecular excimer with substantial CT component. This CT character is due to mixed FE/CT state according to the established description of π-stacked PBI dimers.[31,46,47] The residual monomer-like emission around 525 nm verified by excitation spectra (Fig. S6) is more pronounced for **CF(4)** than for **CF(7)**, suggesting that the larger rotational angle in **CF(4)** weakens ground-state interaction and leads to a greater population of unfolded or loosely folded conformations. Furthermore, **CF(7)** exhibits a structured excimer emission band with two discernible local maxima, which likely reflects the conformational heterogeneity and solvent-induced perturbations within the excimer manifold, arising from the greater flexibility introduced by the longer alkyl chain between the π-units.[48–50]

Surprisingly, despite the structural and coupling differences, both **CF(4)** and **CF(7)** exhibit high photoluminescence quantum yields (PLQYs, Table S4), even subtracting the contribution of the unfolded conformation from the approximation. In TOL, the PLQYs of the two foldamers reach ~20%, comparable to that of the Ref ($\Phi_{Ref} = 25.8\%$). Such efficient excimer emission is uncommon,[51,52] especially for the PBI-based systems, where excimers typically show PLQYs lower than 5% even when the monomer emits with near-unity efficiency.[25,50] The outstanding emission properties of these cross foldamers are attributed primarily to the suppression of nonradiative decay pathways (Table S5), implying distinct excited-state dynamics that will be

discussed in the following sections. Overall, the predominance of excimer emission in both systems highlights how the rotational arrangement effectively governs the photophysical behavior of the dimers.

When the solvent was changed from TOL to $CHCl_3$, the absorption profiles of both **CF(4)** and **CF(7)** show only minor variations, indicating that their ground-state geometries are not strongly perturbed under these two conditions (Fig. S3a). By contrast, the emission spectra exhibit distinct changes (Fig. S3b). The monomer-like emission band of **CF(4)** decreased from TOL to $CHCl_3$, whereas that of **CF(7)** increased noticeably. This opposite response suggests that the excited-state interactions in the two dimers are sensitive to the dielectric environment. Despite these spectral changes, both foldamers remain relatively high PLQYs even in the polar solvent $CHCl_3$ (Table S4), underscoring the robustness of their emissive properties across the two environments tested.

Ultrafast dynamics and relaxation processes

To acquire an in-depth understanding of excimer-mediated excited-state dynamics, solvent-dependent femtosecond transient absorption (fsTA) measurements were employed for **CF(4)**, **CF(7)**, and Ref. The pump wavelength (500 nm) was chosen to coincide with the 0–0 absorption band so that the observed dynamics report on relaxation within the lowest excited-state manifold. In the following discussion, we adopt a diabatic-basis representation, in which the relevant excited-state manifold of the foldamers is treated as adiabatic mixed states expressed as coherent superpositions of Frenkel exciton $|^1(S_1S_0)\rangle$, charge-transfer $|CT\rangle$, excimer $|Ex\rangle$, and correlated triplet pair $|^1(T_1T_1)\rangle$.[22,53] For PBI derivatives, the excimer $|Ex\rangle$ also represents a strongly mixed state with substantial contributions from $|^1(S_1S_0)\rangle$ and $|CT\rangle$. The experimentally observed species in cross foldamers are therefore not pure electronic states but adiabatic mixtures whose composition evolves along the excited-state relaxation coordinate.

The 2D heatmaps of the Ref in TOL (Fig. 3a) provide a clear reference for subsequent foldamers analysis. Immediately following 500 nm excitation, the transient spectrum exhibits ground-state bleach (GSB) and stimulated emission (SE) bands between 450–590 nm, along with a sharp excited-state absorption (ESA) at ~650 nm, collectively confirming the population of the FE state. Subsequently, a red shift of the negative bands and a blue shift/weakening of the ESA occur within tens of picoseconds, indicating structural relaxation in the singlet manifold. Finally, a new absorption feature emerges near 550 nm, accompanied by an isosbestic point at ~600 nm and the decay of FE-related signals, signifying triplet formation *via*

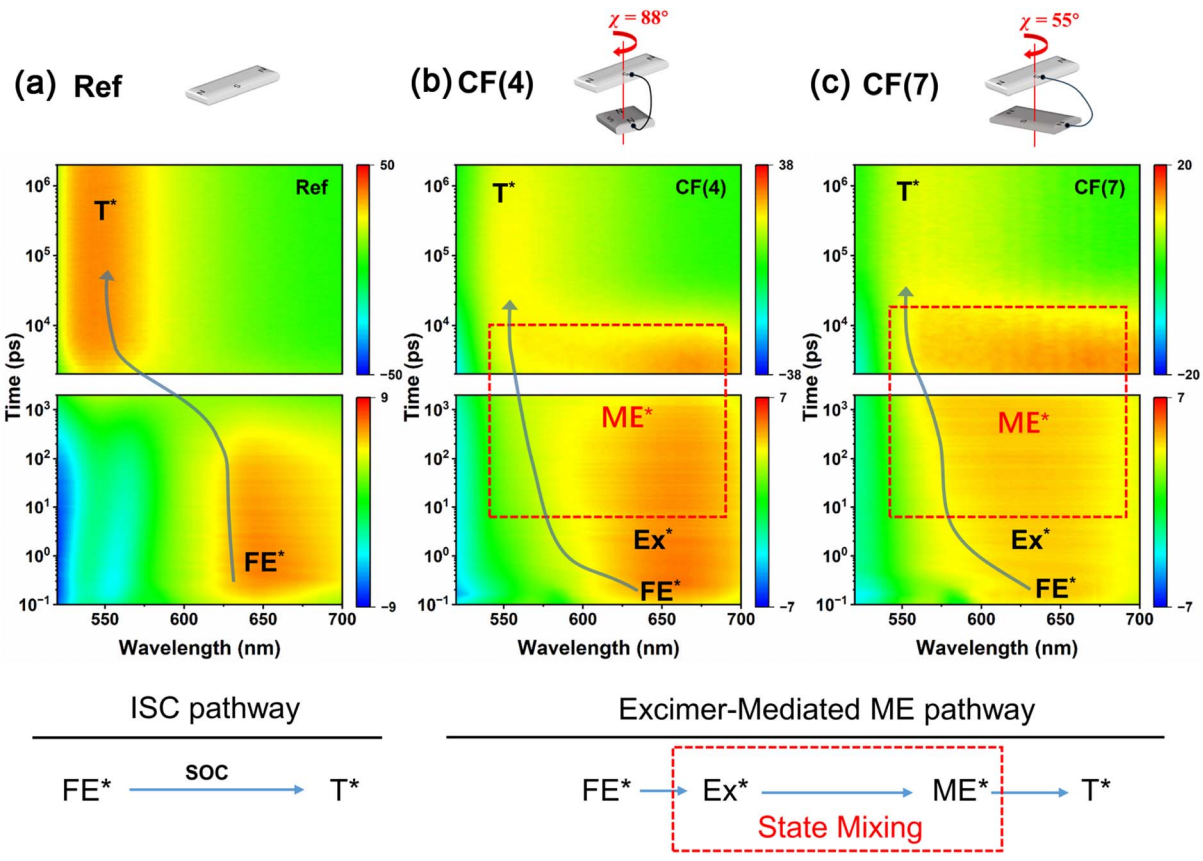

Fig. 3 2D heatmaps in TOL at fs and ns timescales, which show different pathways for (a) Ref, (b) **CF(4)**, and (c) **CF(7)**. For Ref, a simple transition from FE to T occurs through the ISC pathway without any mixed state. For foldamers **CF(4)** and **CF(7)**, the triplet state comes from FE → Ex → ME → T pathway through the mixed state, suggesting the excimer-mediated ME process.

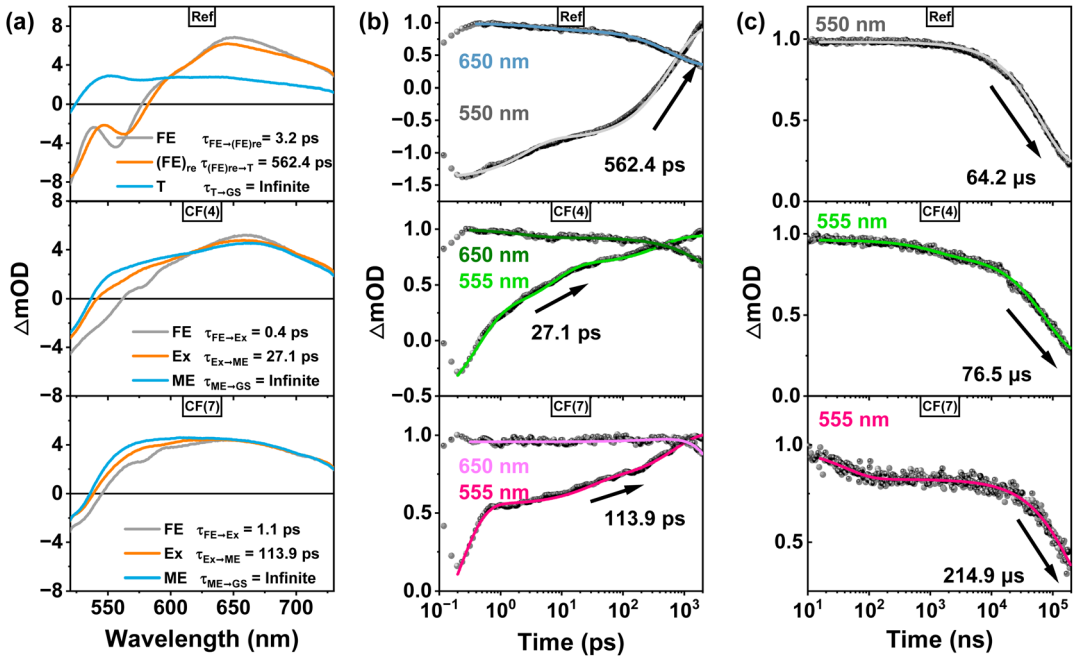

Fig. 4 (a) Evolution-associated spectra obtained from global analysis of fsTA illustrate the pathway, together with the extracted lifetimes for the Ref (top), **CF(4)** (middle), and **CF(7)** (bottom). Kinetic traces at 550 nm for T or 555 nm for ME and 650 nm for FE or Ex at (b) fs and (c) ns timescales for the Ref (top), **CF(4)** (middle), and **CF(7)** (bottom).

intersystem crossing (ISC) (Fig. S9a). Global analysis resolves three species: the pump-initiated FE ($\tau_1 = 3.2$ ps), a relaxed FE ($\tau_2 = 562.4$ ps), and a triplet state, where the 650 nm ESA persists weakly while the 550 nm band becomes dominant (Fig. 4a, top). The transition is marked by a decay of the ~650 nm ESA and a concurrent rise of the 550 nm absorption, consistent with ISC. This assignment is further supported by nanosecond transient absorption (nsTA) data (Fig. S10a and b), which show continuous growth of the 550 nm band alongside decay at 660 nm. A similar triplet formation pathway occurs more rapidly for the Ref in $CHCl_3$ (Fig. S9b, S10c and d) compared to TOL (414.5 ps *vs.* 562 ps). Given the limited solvent range accessible for the systems, we describe this difference as a solvent-sensitive variation under the two tested conditions.

For the **CF(4)** and **CF(7)**, whose coupling strength is modulated by the alkyl chains, different excited-state dynamics were monitored. The 2D heatmaps of **CF(4)** in TOL (Fig. 3b) exhibit GSB between 450–550 nm and a sharp ESA at ~650 nm, closely resembling the initial spectral profile of the Ref and confirming the photoinitiated FE state. This ESA subsequently broadens into a featureless band within picoseconds, reflecting the rapid collapse of the wavefunction into an excimer state. A new ESA band then emerges at ~555 nm. In previous studies,[8,12,49] the excimer-mediated processes were also assigned based on the characteristic fsTA signatures, namely the rapid transformation of a sharp FE-like ESA into a broad excimer-associated band. Global analysis (Fig. 4a, middle) resolves three species: the initial FE ($\tau_1 = 0.5$ ps), a structurally relaxed Ex ($\tau_2 = 27.1$ ps), and a long-lived state characterized by the coexistence of the 555 nm band and residual 660 nm ESA. We refer to this long-lived mixed excited-state as a ME state with $|^1(T_1T_1)\rangle$ dominant character. The extended lifetime of ME state, as confirmed by nsTA measurements (Fig. S11b and c), supports its assignment as an ME state formed *via* excimer-mediated ME. Based on the previous reports, for PBI derivatives, TT manifests as bands near 550 nm on a timescale significantly shorter than ISC-driven triplet formation, also similarly consistent with our findings.[3,24,54,55]

Although both Ref and **CF(4)** exhibit similar spectral signatures immediately after excitation—GSB in the 450–550 nm range and a sharp ESA at 650 nm—their subsequent excited-state evolution diverges significantly (Fig. 4a and b). In Ref, the initially populated FE undergoes structural relaxation within the singlet manifold and subsequently converts into the triplet state *via* ISC on a hundreds-of-picoseconds timescale. By contrast, **CF(4)** displays a rapid transformation of the initially localized FE into a structurally relaxed excimer state within a few picoseconds, as evidenced by the pronounced broadening and red-shift of the 650 nm ESA. This excimer does not represent a pure electronic state, but rather a strongly mixed configuration with substantial contributions from the FE and CT diabatic states. This intermediate subsequently evolves into a ME state, as evidenced by the rise of the 555 nm absorption band associated with increasing triplet components. It is important to note that the ME state here does not represent a pure TT alone, but rather a mixed electronic configuration that retains contributions from all three diabatic components described earlier, *i.e.*, the FE, CT and TT. The interpretation is supported by the global analysis, which shows that the final fitted spectrum of ME state contains spectral signatures associated with these components. Such a multiconfigurational nature reflects the strongly coupled manifold of excited states in

CF(4) and highlights that SF proceeds not through a discrete state-to-state transition, but *via* an adiabatic evolution of the wavefunction across this mixed-state landscape.

Importantly, the 555 nm feature observed for **CF(4)** differs from the triplet absorption spectrum of Ref, combined with the distinct kinetic formation and the excimer-mediated sequential evolution (*vide infra*), indicating a fundamentally distinct photophysical origin. We note, however, that prior studies have shown that markedly faster triplet formation in certain covalent dimers can still arise from enhanced ISC enabled by near-degenerate energetics; thus, a simple rate acceleration in the dimer is not, by itself, diagnostic of SF.[56] In the present case, the assignment is instead anchored by the spectral comparison: the transient signatures of ME for **CF(4)** are clearly distinct from those of the Ref triplet and include features not observed in the triplet spectrum. Coupled with the rapid appearance of the multiexcitonic state in **CF(4)** (∼27 ps), which is more than an order of magnitude faster than the ISC-generated triplet in Ref (∼562 ps), these data provide strong support for excimer-mediated ME pathway. This conclusion is further supported by kinetic traces from fsTA and nsTA (Fig. 4b, S10b and S11c), which show asynchronous dynamics: while in Ref the decay of the ∼660 nm ESA coincides with the rise of the 550 nm triplet band (typical of ISC), in **CF(4)** the 555 nm band exhibits a delayed growth relative to the 660 nm decay. This temporal offset indicates a sequential mechanism in which the FE first relaxes into an excimer state that subsequently serves as a precursor to the correlated triplet pair, rather than a direct ISC pathway. Additional insights are obtained from the spectral evolution on the nanosecond timescale (Fig. S11b). The initial nsTA spectrum of **CF(4)** preserves both the 660 nm and 555 nm bands observed at the end of the fsTA window. Over time, the 555 nm feature gradually intensifies without completely replacing the 660 nm band, reflecting the mixed electronic character of the ME state. Decay kinetics further underscore the distinct nature of this state (Fig. 4c). While the monomer triplet in Ref decays monoexponentially (τ = 64.2 μs), **CF(4)** exhibits a decay with lifetime comparable to the intrinsic triplet lifetime (τ = 76.5 μs). Moreover, subtle but persistent differences in the nsTA spectral profile between **CF(4)** and Ref (Fig. S17) further support the multiconfigurational nature of the excimer-mediated ME state, consistent with previous observations.[2] While a CT-mediated ISC contribution may exist as a parallel channel, the present data do not support assigning it as the dominant origin of the long-lived state in crossfoldamers.[57] Spin evolution within the correlated triplet-pair manifold prior to dissociation may involve mixing among ^{1}(TT), ^{3}(TT), and ^{5}(TT) states, as reported in previous studies; however, such multiplicity assignments cannot be resolved here in the absence of spin-sensitive measurements.[58,59]

CF(7), by contrast, exhibits markedly different dynamics due to its smaller rotational angle (55°) and stronger coupling (Fig. S16). The fsTA spectra in TOL (Fig. 3c) reveal a broader initial ESA than that of **CF(4)**, indicating enhanced delocalization and stronger FE-CT admixture at early times. Global fitting (Fig. 4a, bottom) yields the same sequence of species—FE, Ex, and ME—but all transitions occur more slowly. The formation of the ME state proceeds on a timescale of 113.9 ps, compared with 27.1 ps in **CF(4)**. This interpretation is supported by nsTA data (Fig. S12), which show delayed development of the 555 nm band and a longer triplet lifetime (τ = 214.9 μs) relative to **CF(4)** (Fig. 4c).

The key reason for these differences lies in a smaller rotation and stronger coupling for **CF(7)** relative to **CF(4)**. From an energetic perspective, the larger π-overlap area in **CF(7)** facilitates the formation of a more stabilized excimer configuration, while its stronger coupling further stabilizes the CT component within the excimer. This results in a deeper excimer potential well compared to **CF(4)**, making the excimer state more stable and increasing the reorganization energy required for the transition to the ME state. Consequently, both the formation and dissociation rates of the ME state become slower in **CF(7)**. From a wavefunction perspective, the deeper excimer potential in **CF(7)** can be attributed to its substantially larger CT coupling (J_{CT} = 323 cm^{-1}), which increases the CT weight in the excimer wavefunction relative to **CF(4)**. This, in turn, makes it more difficult to collapse into the TT configuration within the mixed state. As a result, the excimer in **CF(7)** is more CT-like (higher $|CT\rangle$ components), whereas that in **CF(4)** retains larger $|^1(S_1S_0)\rangle$ components. The slower kinetics for the ME generation process in **CF(7)** reveal an important structure–function relationship: the increased CT admixture and deeper excimer basin impose a higher reorganization barrier for accessing the correlated triplet-pair configuration, thereby slowing the adiabatic evolution toward the ME state. By contrast, the weaker and partially cancelling coulombic and CT couplings in **CF(4)** yield a shallower excimer potential, facilitating more rapid wavefunction reconfiguration toward ME. The results highlight that SF kinetics are optimized not by maximizing coupling, but by achieving a balanced mixing of FE and CT character that minimizes excimer stabilization while preserving sufficient coupling to TT manifold.

In polar $CHCl_3$, the excited-state dynamics of **CF(4)** and **CF(7)** remain qualitatively similar to those in TOL, though with notable solvent-induced modifications (Fig. S13–S15 and Table S6). The initial ESA appears red-shifted and sharper near 675 nm, which may indicate partial decoupling of the FE and CT states due to the differential stabilization in the polar medium $CHCl_3$. This is followed by accelerated excimer formation with rapid spectral broadening, while maintaining the same excimer-mediated ME pathway, as confirmed by the persistent spectral features in nsTA. In this context, polar medium $CHCl_3$ consistent with solvent tuning that may preferentially stabilize the CT component of the excimer, thereby modestly accelerating ME formation. However, the intrinsic capacity to undergo excimer-mediated ME remains governed by the molecular architecture—specifically, the chromophore orientation and strength of coupling.

The triplet quantum yields were evaluated using the comparative method based on singlet oxygen generation (details in SI, Table S7 and Fig. S18). The determined quantum yields for singlet oxygen of Ref, **CF(4)**, and **CF(7)** are 0.626, 0.575, and 0.645 in TOL. For Ref, the high triplet yield arises primarily from ISC, facilitated by the heavy-atom effect of the

sulfur atom, and is significantly higher than that of non-heavy-atom-containing PBI analogues.[55] For **CF(4)** and **CF(7)**, the overall triplet yields are comparable to that of the Ref, but their origin differs fundamentally. As discussed above, the dominant pathway for generating the new long-lived species in **CF(4)** and **CF(7)** is excimer-mediated ME, as evidenced by their ESA signatures, which differ markedly from the triplet absorption profile of the Ref. Nevertheless, ISC contributes to some extent in the dimers, as indicated by minor spectral components resembling the monomer triplet; however, this pathway is not dominant, since even at 100 μs, the spectra of **CF(4)** and **CF(7)** remain distinct from the Ref (Fig. S17). Furthermore, the slightly higher singlet oxygen yield of **CF(7)** compared to **CF(4)** may reflect two contributing factors. First, spectral deconvolution and excitation analyses (Fig. S7) indicate a higher folded population for **CF(7)** under our conditions, such that a larger fraction of the excited ensemble accesses the intramolecular excimer/ME manifold. Second, the more pronounced CT component in **CF(7)** can modulate state mixing and pathway branching within this manifold,[22] thereby influencing the net population of oxygen-sensitizing triplet-related products. Notably, the difference in singlet oxygen yields is modest, and this trend is therefore interpreted cautiously. Furthermore, the triplet yield is also analysed using the GSB recovery method, and a consistent trend was obtained, which supported the results of the singlet oxygen yields (Fig. S19 and Table S8).

Together with the solvent- and yield-dependent analysis, the results delineate the underlying structure–function correlation in the foldamers (Fig. 5). The observations highlight the cooperative roles of coupling and chromophore orientation in dictating excited-states evolution. **CF(4)**, with nearly orthogonal chromophores ($\chi = 88°$) and partially cancelling coulombic and CT contributions ($J_{Tot} = -40$ cm^{-1}), exhibits a shallow excimer basin and reaches the ME state rapidly. By contrast, **CF(7)**, with strong coupling ($J_{Tot} = +719$ cm^{-1}) enabled by a longer alkyl chain, stabilizes the excimer in a deeper energetic minimum that imposes a kinetic bottleneck for ME formation. Solvent polarity further modulates the pathways by stabilizing CT character and promoting structural relaxation, accelerating excimer formation while amplifying the differences between the two foldamers. On the microsecond timescale, both systems ultimately display a persistent absorption at ~550 nm attributed to TT component, but its separation efficiency difference can be rationalized by the stronger coupling and reduced rotation in **CF(7)**, which enhance initial CT admixture and facilitate partial localization of TT prior to recombination, thus **CF(7)** exhibits slightly more efficient population of free or weakly bound triplets relative to **CF(4)**. Collectively, the results reveal that the interplay of coulombic and CT interactions with geometric constraints governs not only excimer formation and SF kinetics but also the stability and separation efficiency of TT states, offering critical design principles for developing high-performance SF chromophore assemblies.

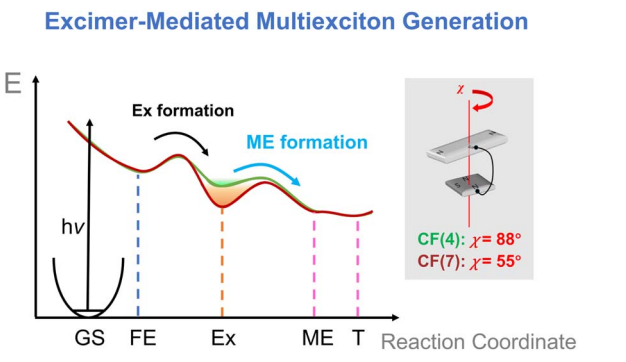

Fig. 5 Schematic of excimer-mediated ME generation and potential-energy profiles along the reaction coordinate for CF(4) (green) and CF(7) (red), illustrating conversion from the FE to Ex (black arrow), and subsequent ME generation (blue arrow), finally decomposed into T. Inset model highlights the rotational angle (χ) for CF(4) and CF(7).

Conclusion

In summary, we have demonstrated that the rotational angle between the two conjugated units in covalently linked cross foldamers serves as a decisive structural parameter for modulating coupling, excimer energetics, and the kinetics of ME formation. By synthesizing two thiophene-fused PBI dimers, **CF(4)** ($\chi = 88°$) and **CF(7)** ($\chi = 55°$), we established a well-defined model system in which the π–π stacking distance is held constant while the rotational angle is systematically varied *via* alkyl-chain engineering. The controlled geometric variation directly dictates the magnitude and sign of the total coupling. The nearly orthogonal geometry of **CF(4)** results in weak, near-zero coupling, whereas the less rotational arrangement of **CF(7)** produces strong, positive coupling. These differences in coupling are reflected in the steady-state photophysics: both foldamers form excimers that emit with unusually high quantum yields (~20%), but their excited-state landscapes differ substantially. Ultrafast spectroscopy reveals that both systems undergo excimer-mediated ME formation, yet with starkly different dynamics. In weakly coupled **CF(4)**, the excimer forms rapidly and serves as a shallow, mixed state that facilitates fast evolution into the ME state within ~27 ps. By contrast, the strongly coupled **CF(7)** forms a more stabilized excimer with greater CT character, creating a deeper potential well that slows the formation of the ME state to ~114 ps. Solvent polarity further modulates the pathways by selectively stabilizing the CT component, accelerating excimer formation but preserving the fundamental angle-dependent dynamic hierarchy.

Overall, the results establish a clear, causal structure–dynamics relationship: the rotational angle controls the coupling and dimeric structure, which in turn governs the rate of ME state formation. Beyond this specific system, this study provides a general design strategy for controlling ME processes in π-conjugated assemblies.

Author contributions

W. Li and W. Zhang contributed equally to this work. W. Li performed the synthesis and characterizations. W. Li and L. Liu analysed the steady-state spectroscopy data. W. Zhang and H. Song were responsible for the transient absorption experiments

and corresponding analysis. W. Li and J. Zhou carried out the theoretical calculations. W. Li and W. Zhang drafted the manuscript, and all authors revised it critically. Z. Xie supervised the entire project. All the authors have given approved the final version of the manuscript.

Conflicts of interest

There are no conflicts to declare.

Data availability

All data supporting this study are available from article and supplementary information (SI). Supplementary information: experimental details, synthesis and characterization, DFT calculations, steady-state and transient spectra, singlet oxygen generation experiments. See DOI: https://doi.org/10.1039/d6sc00414h.

Acknowledgements

The authors acknowledge the financing support by the National Natural Science Foundation of China (52373178, 52273178, 22575090, 22503033), the National Key Research and Development Program of China (2022YFA1204404), and the Fund of the Key Laboratory of Luminescence from Molecular Aggregates of Guangdong Province (2023B1212060003). The authors also thank the supporting by State Key Lab of Luminescent Materials and Devices, South China University of Technology (Skllmd-2025–03).

Notes and references

1 R. J. Hudson, T. S. C. MacDonald, J. H. Cole, T. W. Schmidt, T. A. Smith and D. R. McCamey, *Nat. Rev. Chem.*, 2024, **8**, 136–151.
2 W.-L. Chan, M. Ligges, A. Jailaubekov, L. Kaake, L. Miaja-Avila and X.-Y. Zhu, *Science*, 2011, **334**, 1541–1545.
3 A. K. Le, J. A. Bender, D. H. Arias, D. E. Cotton, J. C. Johnson and S. T. Roberts, *J. Am. Chem. Soc.*, 2018, **140**, 814–826.
4 A. B. Pun, A. Asadpoordarvish, E. Kumarasamy, M. J. Y. Tayebjee, D. Niesner, D. R. McCamey, S. N. Sanders, L. M. Campos and M. Y. Sfeir, *Nat. Chem.*, 2019, **11**, 821–828.
5 K. R. Parenti, R. Chesler, G. He, P. Bhattacharyya, B. Xiao, H. Huang, D. Malinowski, J. Zhang, X. Yin, A. Shukla, S. Mazumdar, M. Y. Sfeir and L. M. Campos, *Nat. Chem.*, 2023, **15**, 339–346.
6 D. Thiel, H. Gotfredsen, P. M. Greißel, L. Chen, M. Krug, I. Papadopoulos, M. J. Ferguson, T. Torres, T. Clark, C. Neiss, A. Görling, M. B. Nielsen, R. R. Tykwinski and D. M. Guldi, *J. Am. Chem. Soc.*, 2025, **147**, 32124–32144.
7 S. R. Yost, J. Lee, M. W. B. Wilson, T. Wu, D. P. McMahon, R. R. Parkhurst, N. J. Thompson, D. N. Congreve, A. Rao, K. Johnson, M. Y. Sfeir, M. G. Bawendi, T. M. Swager, R. H. Friend, M. A. Baldo and T. Van Voorhis, *Nat. Chem.*, 2014, **6**, 492–497.
8 Y. Hong, J. Kim, W. Kim, C. Kaufmann, H. Kim, F. Würthner and D. Kim, *J. Am. Chem. Soc.*, 2020, **142**, 7845–7857.
9 E. A. Margulies, C. E. Miller, Y. Wu, L. Ma, G. C. Schatz, R. M. Young and M. R. Wasielewski, *Nat. Chem.*, 2016, **8**, 1120–1125.
10 D. R. Maslennikov, M. Maimaris, H. Ning, X. Zheng, N. Mondal, V. V. Bruevich, S. M. Pratik, Y. Dong, J. W. G. Tisch, A. J. Musser, V. Podzorov, J.-L. Bredas, V. Coropceanu and A. A. Bakulin, *J. Am. Chem. Soc.*, 2025, **147**, 23536–23544.
11 J. Kim, D. C. Bain, V. Ding, K. Majumder, D. Windemuller, J. Feng, J. Wu, S. Patil, J. Anthony, W. Kim and A. J. Musser, *Nat. Chem.*, 2024, **16**, 1680–1686.
12 J. Sung, A. Nowak-Krol, F. Schlosser, B. Fimmel, W. Kim, D. Kim and F. Würthner, *J. Am. Chem. Soc.*, 2016, **138**, 9029–9032.
13 D. Chaudhuri, *Org. Mater.*, 2021, **3**, 455–468.
14 C. B. Dover, J. K. Gallaher, L. Frazer, P. C. Tapping, A. J. Petty, M. J. Crossley, J. E. Anthony, T. W. Kee and T. W. Schmidt, *Nat. Chem.*, 2018, **10**, 305–310.
15 C. M. Mauck, P. E. Hartnett, E. A. Margulies, L. Ma, C. E. Miller, G. C. Schatz, T. J. Marks and M. R. Wasielewski, *J. Am. Chem. Soc.*, 2016, **138**, 11749–11761.
16 L. Wang, W. Cai, J. Sun, Y. Wu, B. Zhang, X. Tian, S. Guo, W. Liang, H. Fu and J. Yao, *J. Phys. Chem. Lett.*, 2021, **12**, 12276–12282.
17 C. Lin, T. Kim, J. D. Schultz, R. M. Young and M. R. Wasielewski, *Nat. Chem.*, 2022, **14**, 786–793.
18 S. B. Tyndall, J. R. Palmer, N. A. Tcyrulnikov, R. M. Young and M. R. Wasielewski, *J. Phys. Chem. B*, 2025, **129**, 3454–3463.
19 L. Ernst, H. Song, D. Kim and F. Würthner, *Nat. Chem.*, 2025, **17**, 767–776.
20 B. Teichmann, M. Sárosi, K. Shoyama, M. A. Niyas, R. K. Dubey and F. Würthner, *Angew. Chem., Int. Ed.*, 2025, **64**, e202414069.
21 G. Bressan, S. E. Penty, D. Green, I. A. Heisler, G. A. Jones, T. A. Barendt and S. R. Meech, *Angew. Chem., Int. Ed.*, 2024, **63**, e202407242.
22 R. M. Young and M. R. Wasielewski, *Acc. Chem. Res.*, 2020, **53**, 1957–1968.
23 N. J. Hestand and F. C. Spano, *Chem. Rev.*, 2018, **118**, 7069–7163.
24 Y. Hong, M. Rudolf, M. Kim, J. Kim, T. Schembri, A.-M. Krause, K. Shoyama, D. Bialas, M. I. S. Röhr, T. Joo, H. Kim, D. Kim and F. Würthner, *Nat. Commun.*, 2022, **13**, 4488.
25 J. M. Giaimo, J. V. Lockard, L. E. Sinks, A. M. Scott, T. M. Wilson and M. R. Wasielewski, *J. Phys. Chem. A*, 2008, **112**, 2322–2330.
26 V. Dehm, M. Büchner, J. Seibt, V. Engel and F. Würthner, *Chem. Sci.*, 2011, **2**, 2094.
27 S. Samanta and D. Chaudhuri, *J. Phys. Chem. Lett.*, 2017, **8**, 3427–3432.
28 S. Sao, S. Naskar, N. Mukhopadhyay, M. Das and D. Chaudhuri, *Chem. Commun.*, 2018, **54**, 12186–12189.

29 K. M. Lefler, K. E. Brown, W. A. Salamant, S. M. Dyar, K. E. Knowles and M. R. Wasielewski, *J. Phys. Chem. A*, 2013, **117**, 10333–10345.
30 H. Liu, L. Shen, Z. Cao and X. Li, *Phys. Chem. Chem. Phys.*, 2014, **16**, 16399–16406.
31 E. A. Margulies, L. E. Shoer, S. W. Eaton and M. R. Wasielewski, *Phys. Chem. Chem. Phys.*, 2014, **16**, 23735–23742.
32 J. Zhou, W. Zhang, X.-F. Jiang, C. Wang, X. Zhou, B. Xu, L. Liu, Z. Xie and Y. Ma, *J. Phys. Chem. Lett.*, 2018, **9**, 596–600.
33 N. Tang, J. Zhou, L. Wang, M. Stolte, G. Xie, X. Wen, L. Liu, F. Würthner, J. Gierschner and Z. Xie, *Nat. Commun.*, 2023, **14**, 1922.
34 C. Kaufmann, D. Bialas, M. Stolte and F. Würthner, *J. Am. Chem. Soc.*, 2018, **140**, 9986–9995.
35 E. Sebastian, A. M. Philip, A. Benny and M. Hariharan, *Angew. Chem., Int. Ed.*, 2018, **57**, 15696–15701.
36 L. Ma, Y. Liu, Y. Zhao, X. Sun, Y. Zhang, A. Yin, D. Cao, Q. Chen and G. Gao, *Appl. Surf. Sci.*, 2023, **616**, 156422.
37 W. Li and Z. Xie, *Chem.–Eur. J.*, 2025, **31**, e202403908.
38 Z. Xie, B. Yang, F. Li, G. Cheng, L. Liu, G. Yang, H. Xu, L. Ye, M. Hanif, S. Liu, D. Ma and Y. Ma, *J. Am. Chem. Soc.*, 2005, **127**, 14152–14153.
39 E. A. Margulies, J. L. Logsdon, C. E. Miller, L. Ma, E. Simonoff, R. M. Young, G. C. Schatz and M. R. Wasielewski, *J. Am. Chem. Soc.*, 2017, **139**, 663–671.
40 S. D. Jadhav, D. Sasikumar and M. Hariharan, *Phys. Chem. Chem. Phys.*, 2022, **24**, 16193–16199.
41 E. A. Strømsodd, A. F. Buene, D. M. Almenningen, O. R. Gautun and B. H. Hoff, *Dyes Pigm.*, 2023, **209**, 110899.
42 Y. Li, W. Xu, S. D. Motta, F. Negri, D. Zhu and Z. Wang, *Chem. Commun.*, 2012, **48**, 8204–8206.
43 N. J. Hestand and F. C. Spano, *J. Chem. Phys.*, 2015, **143**, 244707.
44 M. P. Lijina, A. Benny, R. Ramakrishnan, N. G. Nair and M. Hariharan, *J. Am. Chem. Soc.*, 2020, **142**, 17393–17402.
45 M. P. Lijina, A. Benny, E. Sebastian and M. Hariharan, *Chem. Soc. Rev.*, 2023, **52**, 6664–6679.
46 Y. Hong, W. Kim, T. Kim, C. Kaufmann, H. Kim, F. Wurthner and D. Kim, *Angew. Chem., Int. Ed.*, 2022, **61**, 8.
47 Y. Hong, F. Schlosser, W. Kim, F. Würthner and D. Kim, *J. Am. Chem. Soc.*, 2022, **144**, 15539–15548.
48 E. Sebastian, J. Sunny and M. Hariharan, *Chem. Sci.*, 2022, **13**, 10824–10835.
49 W. Zhang, B. Teichmann, Y. Park, Y. M. Jung, B. Liu, F. Würthner and D. Kim, *J. Am. Chem. Soc.*, 2026, **148**, 5476–5485.
50 K. E. Brown, W. A. Salamant, L. E. Shoer, R. M. Young and M. R. Wasielewski, *J. Phys. Chem. Lett.*, 2014, **5**, 2588–2593.
51 H. Liu, Y. Gu, Y. Dai, K. Wang, S. Zhang, G. Chen, B. Zou and B. Yang, *J. Am. Chem. Soc.*, 2020, **142**, 1153–1158.
52 S. Wang, H. Liu, S. Zhao, Q. Wu, Z. Yang, D. Yang, Y. Lv, Q. Su, S.-T. Zhang and B. Yang, *Chem. Sci.*, 2025, **16**, 3275–3284.
53 J. D. Schultz, J. L. Yuly, E. A. Arsenault, K. Parker, S. N. Chowdhury, R. Dani, S. Kundu, H. Nuomin, Z. Zhang, J. Valdiviezo, P. Zhang, K. Orcutt, S. J. Jang, G. R. Fleming, N. Makri, J. P. Ogilvie, M. J. Therien, M. R. Wasielewski and D. N. Beratan, *Chem. Rev.*, 2024, **124**, 11641–11766.
54 M. H. Farag and A. I. Krylov, *J. Phys. Chem. C*, 2018, **122**, 25753–25763.
55 J. Sunny, E. Sebastian, S. Sujilkumar, F. Würthner, B. Engels and M. Hariharan, *Phys. Chem. Chem. Phys.*, 2023, **25**, 28428–28436.
56 G. He, K. R. Parenti, P. J. Budden, J. Niklas, T. Macdonald, E. Kumarasamy, X. Chen, X. Yin, D. R. McCamey, O. G. Poluektov, L. M. Campos and M. Y. Sfeir, *J. Am. Chem. Soc.*, 2023, **145**, 22058–22068.
57 J. Gorman, S. R. E. Orsborne, A. Sridhar, R. Pandya, P. Budden, A. Ohmann, N. A. Panjwani, Y. Liu, J. L. Greenfield, S. Dowland, V. Gray, S. T. J. Ryan, S. De Ornellas, A. H. El-Sagheer, T. Brown, J. R. Nitschke, J. Behrends, U. F. Keyser, A. Rao, R. Collepardo-Guevara, E. Stulz, R. H. Friend and F. Auras, *J. Am. Chem. Soc.*, 2022, **144**, 368–376.
58 M. J. Y. Tayebjee, S. N. Sanders, E. Kumarasamy, L. M. Campos, M. Y. Sfeir and D. R. McCamey, *Nat. Phys.*, 2017, **13**, 182–188.
59 L. R. Weiss, S. L. Bayliss, F. Kraffert, K. J. Thorley, J. E. Anthony, R. Bittl, R. H. Friend, A. Rao, N. C. Greenham and J. Behrends, *Nat. Phys.*, 2017, **13**, 176–181.